

Highly Crystalline Prussian Blue for Kinetics Enhanced Potassium Storage

Wenli Shu, Meng Huang,* Lishan Geng, Fan Qiao, and Xuanpeng Wang*

Prussian blue analogs (PBAs) are promising cathode materials for potassium-ion batteries (KIBs) owing to their large open framework structure. As the K^+ migration rate and storage sites rely highly on the periodic lattice arrangement, it is rather important to guarantee the high crystallinity of PBAs. Herein, highly crystalline $K_2Fe[Fe(CN)_6]$ (KFeHCF-E) is synthesized by coprecipitation, adopting the ethylenediaminetetraacetic acid dipotassium salt as a chelating agent. As a result, an excellent rate capability and ultra-long lifespan (5000 cycles at 100 mA g^{-1} with 61.3% capacity maintenance) are achieved when tested in KIBs. The highest K^+ migration rate of 10^{-9} $cm^2 s^{-1}$ in the bulk phase is determined by the galvanostatic intermittent titration technique. Remarkably, the robust lattice structure and reversible solid-phase K^+ storage mechanism of KFeHCF-E are proved by in situ XRD. This work offers a simple crystallinity optimization method for developing high-performance PBAs cathode materials in advanced KIBs.

1. Introduction

In recent decades, due to the increasing energy crises and environmental pollution, it has become increasingly necessary to develop clean and renewable energies.^[1–3] However, renewable energy sources, such as wind, solar, tide, etc., are highly environmentally dependent. Therefore, the search for efficient energy storage systems to store these renewable energies is urgent. Rechargeable lithium-ion batteries (LIBs) were commercialized by Sony Corporation in 1991. Nowadays, LIBs dominate the market shares of smart electronic devices and electric vehicles due to their high energy density.^[4,5] Unfortunately, the

resource shortages and uneven dispersion of lithium and cobalt are not sufficient to meet the growing demands in grid-scale energy storage.^[6–9] Hence, some promising alternatives, including sodium-ion batteries (NIBs), potassium ion batteries (KIBs), and multivalent metal ion batteries have gained increasing attention.^[10–13] Relatively, KIBs are superior to other alternatives because of more abundant potassium reserves, lower cost, and lower redox potential (−2.93 V vs SHE) of K^+/K .^[14–17] In addition, K^+ has the smallest Stoke radius after solvation compared to Li^+ and Na^+ , and therefore has the highest ionic conductivity and fastest ionic transport. As a result, low-cost KIB is a promising large-scale energy storage technology.^[18–20]


So far, many advances have been made for KIBs in the research of cathode materials, including layered metal oxides,^[21,22] polyanionic compounds^[23,24] and Prussian blue analogs (PBAs),^[25–31] of which PBAs have become the most ideal cathode for KIBs as they have three-dimensional (3D) open-framework structure providing large diffusion channels for K^+ and high theoretical capacity. The layered metal oxides (K_xMnO_2 , birnessite) and polyanionic compounds are both of interest due to their unique structures, but both types of materials face problems such as short cycling life. In contrast, PBAs are inexpensive and offer high specific capacity, high operating voltage, and long cycling life, but their inherent drawbacks of poor electrical conductivity, low density, and inevitable crystal water during synthesis also limit their further development.^[12,14] $K_xM^{II}[M^{III}(CN)_6]_{1-y}\square_\gamma \cdot zH_2O$ ($0 \leq x \leq 2$, $0 \leq \gamma \leq 1$) is the typical formula for potassium-based PBAs, where M and M^0 stand for transition metal ions (Mn, Fe, Ni, Co, etc.), \square stands for $M^0(CN)_6$ vacancies, and H_2O is for interstitial/coordinated water molecules.^[32] However, most reported PBAs showed low capacity and short-term cycling life, because of the high quantity of vacancies and interstitial/coordinated water molecules in their lattice structure, which is due to rapid crystal nucleation and growth.^[33,34] In order to effectively control the crystallization of PBAs, most researchers focused on reducing lattice defects and interstitial water. For instance, Zhu et al. reported defect-free $K_2Mn[Fe(CN)_6]$ which showed a high reversible capacity.^[35] However, Mn-based PBAs are currently restricted from development and practical application because of the Jahn-Teller effect of Mn, causing distortion of the crystal structure and poor cycling stability.^[36] Cao et al. found that $K_{1.81}Ni[Fe(CN)_6]_{0.97} \cdot 0.086H_2O$ exhibits a long cycling life.^[37] Although Ni-based PBAs have few vacancies and coordinated

W. Shu, M. Huang, L. Geng, F. Qiao, X. Wang
School of Materials Science and Engineering, Hainan Institute
Wuhan University of Technology
Wuhan 430070, P.R. China
E-mail: 211808@whut.edu.cn; wxp122525691@whut.edu.cn

W. Shu, M. Huang, X. Wang
Hainan Institute
Wuhan University of Technology
Sanya 572000, P.R. China

X. Wang
Hubei Longzhong Laboratory
Wuhan University of Technology (Xiangyang Demonstration Zone)
Xiangyang 441000, P.R. China

X. Wang
Department of Physical Science & Technology, School of Science
Wuhan University of Technology
Wuhan 430070, P.R. China

 The ORCID identification number(s) for the author(s) of this article can be found under <https://doi.org/10.1002/smll.202207080>.

DOI: 10.1002/smll.202207080

water molecules, hydrothermal preparation is not conducive to large-scale production.^[38] Compared with other PBAs, Fe-based PBAs (Fe-PBAs) consisting of low-cost raw materials and favorable for large-scale application, have become a better choice in KIBs.^[8] Nevertheless, the nano-sized and distorted structure of Fe-PBAs lead to low capacity and short cycle life in practical applications. Therefore, the exploration of simple strategies to synthesize highly crystalline Fe-PBAs to improve the K^+ storage performance is of paramount importance. Moreover, crystallinity, as a key parameter in the crystal structure, is also urgently worth discussing for elucidating the role of dynamic control on the bulk properties of PB materials.

Herein, we report a simple water coprecipitation method to prepare $K_2Fe[Fe(CN)_6]$ (KFeHCF-E) by introducing dipotassium ethylenediaminetetraacetate (EDTA) as a chelating agent. KFeHCF-E has higher crystallinity and higher ion diffusion coefficient than KFeHCF (prepared without EDTA), resulting in ultra-stable cycling capability and enhanced potassium storage kinetics. The obtained KFeHCF-E with robust structure and efficient kinetics shows high cycling stability and rate capability. KFeHCF-E also shows a high initial capacity of 77 mAh g^{-1} at 25 mA g^{-1} . The high reversible capacity is 60.1 mAh g^{-1} at 100 mA g^{-1} and 61.3% of that can be maintained after 5000 cycles. Additionally, the excellent rate performance (a reversible capacity of 48 mAh g^{-1} which is 60.9% of that at 25 mA g^{-1}) and ultra-long lifespan of over 2000 cycles at 1000 mA g^{-1} are acquired. Furthermore, advanced in situ X-ray diffraction (XRD) revealed the highly reversible structure evolution and solid-phase K^+ storage mechanism of KFeHCF-E. This reported highly crystalline PBAs synthesized via a simple method is promising for building low-cost and high-stable KIBs for grid-scale energy storage.

2. Results and Discussion

PBAs are usually synthesized via coprecipitation reaction which occurs rapidly in an uncontrolled manner, leading to the formation of defects and agglomerated particles with a large number of interstitial/coordinated water molecules.^[39–41] To obtain highly crystalline KFeHCF-E, an appropriate amount of chelating agent (EDTA-2K) was added to the aqueous coprecipitation reaction to slow down the crystallization process (Figure 1). The formed EDTA of weak acidity induces

the decomposition of potassium ferricyanide(II) to produce $[Fe(CN)_6]^{4+}$, and $EDTA^{4-}$ has a strong complexing ability for Fe^{2+} . Then, the formed $[Fe(EDTA)]^{2-}$ complexes slowly release Fe^{2+} to largely reduce the reaction between Fe^{2+} and $[Fe(CN)_6]^{4+}$, controlling the nucleation and growth processes to facilitate the formation of highly crystalline PB.^[42,43]

The crystal structures of the as-synthesized KFeHCF-E and KFeHCF were examined by XRD patterns (Figure S1, Supporting Information), and no impure crystalline phases are found. Furthermore, the Rietveld refinement of the XRD data was employed on GSAS software to investigate their crystal structure of the samples (Figures 2a and S2, Supporting Information). As shown in Figure 2a, the sharp XRD peaks demonstrate the well-crystallized monoclinic phase (space group: $P2_1/n$) of KFeHCF-E without any impurities.^[26,44] The detailed refinement results with atomic positions are listed in Table S2 and S3 (Supporting Information), and all fitting good-ness factors (R_{wp} , R_p) display absolutely low values. The results in Tables S2 and S3 (Supporting Information) show that the occupancy of C and N atoms in KFeHCF-E is higher than that in KFeHCF. KFeHCF-E shows only defects of C2 (0.99041) and N2 (0.99041) atoms, while KFeHCF has vacancies in C1 (0.98387), N1 (0.98387), C2 (0.94983), N2 (0.94983), C3 (0.9968) and N3 (0.9968) sites. What's more, the occupancy of O atoms (0.10996) in KFeHCF-E is much lower than that in KFeHCF (0.27261). The above results provide more evidence that KFeHCF-E has a much lower amount of CN defects and interstitial H_2O molecules. The corresponding lattice structure of KFeHCF-E is illustrated in Figure 2b, showing a 3D open framework structure constructed through coordinations between $-CN-$ and Fe cations, and storing K atoms in interstitial sites.

Transmission electron microscopy (TEM) image shows that KFeHCF-E nanoparticles are in the size range of 20–60 nm (Figure 2d) and 55% of that has a number-average width of ~40 nm (Figure S4, Supporting Information), which is beneficial to electrolyte wetting and K^+ access. The corresponding scanning electron microscopy (SEM) images of KFeHCF-E and KFeHCF are displayed in Figure 2c and Figure S5 (Supporting Information), respectively. The smaller size and agglomerated state of KFeHCF imply a more rapid nucleation rate in the absence of EDTA. The Fast Fourier Transform (FFT) pattern (Figure 2e) shows the [100] zone axis of the monoclinic phases, exhibiting a good lattice structure. Three clear lattice fringes of 0.357 nm, 0.252 nm and 0.179 nm derive from the (022), (004)

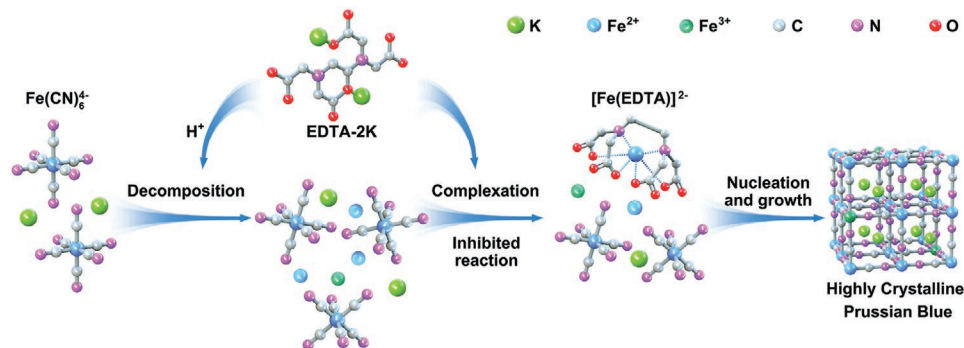


Figure 1. Schematic illustration of coprecipitation synthesis of KFeHCF-E with EDTA chelating agent.

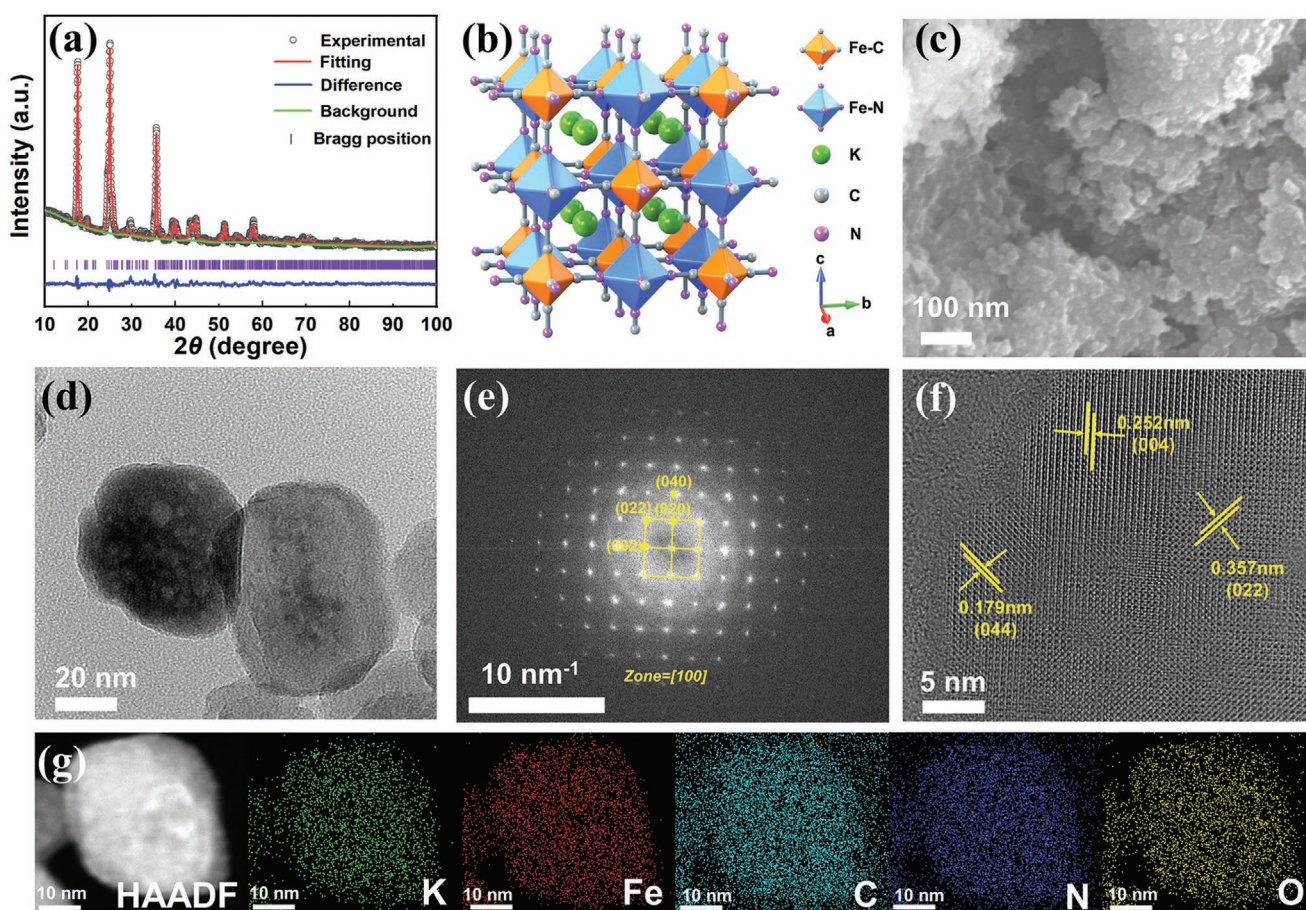


Figure 2. Characterizations of KFeHCF-E: a) Rietveld refinement XRD pattern. b) Corresponding crystal structure model. c) SEM and (d) TEM image of nanoparticles. e) FFT pattern. f) Lattice fringes of crystalline planes. g) HAADF elemental mapping images.

and (044) planes of a monoclinic structure, respectively, further indicating that KFeHCF-E has higher crystallinity (Figure 2f). While the TEM images imply the distorted structure of KFeHCF (Figure S5c,d, Supporting Information). Energy dispersive X-ray spectroscopy (EDS) images demonstrate the uniform distribution of K, Fe, C, N, and O elements (Figure 2g).

As shown in Figure 3a, both KFeHCF-E and KFeHCF are present with K, Fe, C, N, and O elements, detected by X-ray photoelectron spectroscopy (XPS). In the Fe 2p spectrum of KFeHCF-E (Figure 3b), the binding energies of 708.6 and 721.4 eV correspond to Fe_{2p_{3/2}} and Fe_{2p_{1/2}}, respectively, originating from Fe²⁺, and those of 709.3 and 723.0 eV derive from Fe³⁺. The other peaks are the corresponding satellite peaks. In the Raman spectra (Figure 3c), the two peaks located at 2083 and 2121 cm⁻¹ can be assigned to the vibration of Fe²⁺(C≡N) and Fe³⁺(C≡N) bonds, respectively, firmly confirming the coexistence of Fe²⁺ and Fe³⁺ which is consistent with the XPS results.^[39,45] The water content in the samples is determined by thermogravimetric analysis (TGA). Water molecules in the KFeHCF-E and KFeHCF samples are gradually released with the temperature increasing (Figure 3d). Absorbed water molecules are mostly removed below 100°C. The step weight-loss of KFeHCF-E below 200 °C is 2.83% (lower than 4.03% of KFeHCF), which primarily derives from the release of interstitial and coordination

water molecules.^[35] Based on inductively coupled plasma-atomic emission spectrometry (ICP-AES), elemental analysis (Tables S1, Supporting Information) and TGA results, the molecular formulas of KFeHCF-E and KFeHCF are determined as K_{1.61}Fe[Fe(CN)₆]_{0.88}·0.43H₂O and K_{1.51}Fe[Fe(CN)₆]_{0.82}·0.59H₂O, respectively. Due to the low crystal growth rate, KFeHCF-E contains higher K-ion content, lesser [Fe(CN)₆] vacancies and lower water content than KFeHCF.^[46]

Figure 4 displays the electrochemical properties of KFeHCF-E and KFeHCF. The initial cyclic voltammetry (CV) curve of KFeHCF-E shows a pair of well-defined redox peaks (Figure 4a). The much higher peak current of KFeHCF-E than that of KFeHCF suggests the superior K⁺ diffusion kinetics in the lattice structure of KFeHCF-E. The first constant-current charge/discharge curves of KFeHCF-E (3.49/3.35 V) show smaller peak separation compared to KFeHCF (3.53/3.35 V), manifesting superior K⁺ diffusion in KFeHCF-E (Figure 4b). The superior repetition of charge/discharge curves in the initial three cycles manifests the higher reversibility of KFeHCF-E. Figure 4c displays the cycling comparison performance at a low current density of 25 mA g⁻¹. The initial discharge capacity of KFeHCF-E is 77.0 mAh g⁻¹ and an initial Coulombic efficiency (ICE) of 104%, which is higher than that of KFeHCF (71.3 mAh g⁻¹, 93%). Additionally, the capacity of KFeHCF-E maintains

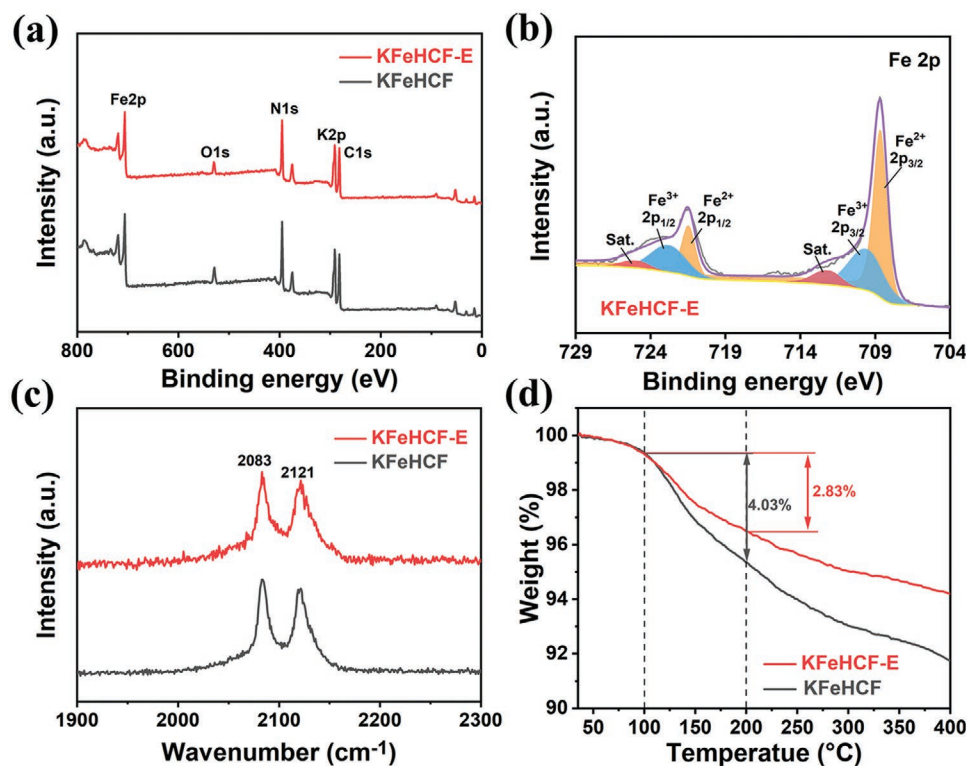


Figure 3. Structural characterization: a) XPS survey spectra. b) Fe 2p fitting spectra of KFeHCF-E. c) Raman spectra. d) TGA comparison curve in N_2 .

at 98.0% which is superior to that (90.3%) of KFeHCF after 30 cycles. In the rate test, KFeHCF-E shows specific capacities of 69, 66, 61, 55, 48, and 42 mAh g^{-1} at 25, 50, 100, 200, 500, and 1000 mA g^{-1} , respectively, corresponding to a high rate retention of 60.9% (Figure 4d). When the current density turns back to 25 mAh g^{-1} , a high rate recovery of 100.6% is obtained. By contrast, KFeHCF shows the low capacity of 68, 60, 43, 25, 14, and 10 mAh g^{-1} at 25, 50, 100, 200, 500, and 1000 mA g^{-1} , respectively, a low rate retention of 14.7%, and a rate recovery of 98%. The corresponding charge/discharge curves are displayed in Figure S7 (Supporting Information). The capacity degradation of both at high current densities derives from mainly voltage polarization, and the KFeHCF-E has a longer discharge plateau and lower average overpotential (0.54 V) than that of KFeHCF (0.61 V) at 1000 mA g^{-1} (Figure S8, Supporting Information). The improved cyclability and rate capability of KFeHCF-E confirm that highly crystalline structure can facilitate structural stability and ionic diffusion. In addition, the KFeHCF-E electrode has an initial capacity of 60.1 mAh g^{-1} at 100 mAh g^{-1} , and 61.3% of that is maintained after cycling 5000 times (running time over 208 days), showing a capacity degradation rate of 0.0077% per time (Figure 4e). The coulombic efficiency is as high as 99.9%, indicating excellent reversibility for K^+ insertion/extraction into/from KFeHCF-E. The corresponding voltage profiles are displayed in Figure 4f and show negligible change after 2000 cycles, revealing the high structural stability of KFeHCF-E during K^+ insertion/extraction. In contrast, the cycling life of fewer than 300 cycles and lower discharge capacity ($< 50 \text{ mAh g}^{-1}$) of KFeHCF demonstrate the importance of the highly crystalline structure of KFeHCF-E ensured

by EDTA modification in enhancing the electrochemical performance. At 200 mA g^{-1} , a discharge capacity of 56.8 mAh g^{-1} is acquired for KFeHCF-E and 87.6% of that is maintained after 3200 cycles (Figure S10, Supporting Information). Note that the fluctuations in Figure 4e are caused by a power failure. At 500 mA g^{-1} , the KFeHCF-E is still able to cycle for 1800 cycles at $\sim 52.3 \text{ mAh g}^{-1}$ (Figure 4g), the corresponding charge/discharge curves are displayed in Figure S11 (Supporting Information). In addition, at a higher current density of 1000 mA g^{-1} , KFeHCF-E can achieve an ultra-long cycling life of 2000 cycles and an average capacity of 49.4 mAh g^{-1} is realized (Figure 4h).

The excellent electrochemical performance of KFeHCF-E relies highly on their highly crystalline structure. In order to further investigate the structural evolution and specific process of K^+ insertion/extraction of KFeHCF-E, in situ XRD characterization was conducted (Figure 5). Figure 5a,b show a slight shift of the peaks of KFeHCF-E at 178° , 25.2° , and 35.9° toward lower angles, revealing that it undergoes small lattice expansion during K^+ extraction. Upon the discharge process, these peaks take the reverse shifting, revealing the highly reversible solid-solution phase energy storage process. KFeHCF-E undergoes small lattice change (1.1%) and cell volume expansion (3.5%) upon K^+ insertion/extraction (Figure 5c), enabling its ultrastable cycling life. In addition, KFeHCF-E cells have a lower increment of charge transfer resistance than KFeHCF cells (Figure S12, Supporting Information), which explains the improved rate performance of KFeHCF-E. Additionally, the CV curves of KFeHCF-E present redox peaks at 3.65/3.09 V, 3.66/3.02 V, 3.67/2.95 V, 3.67/2.92 V, 3.67/2.89 V, and 3.70/2.87 V at different scan rates (Figure S13a, Supporting Information). The peaks

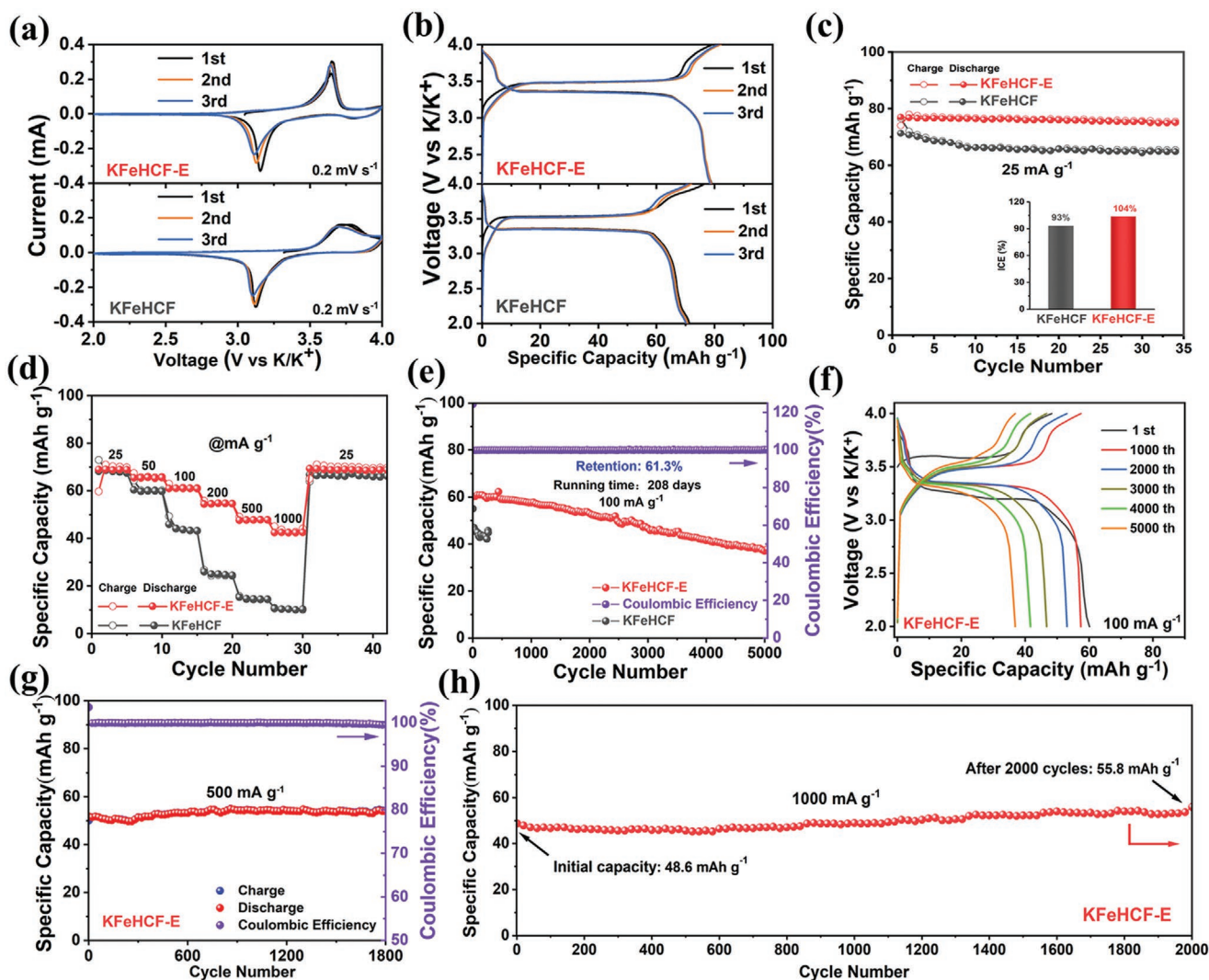


Figure 4. a) CV curves and b) galvanostatic charge/discharge curves of KFeHCF-E and KFeHCF. c) Cycling comparison performance at 25 mA g^{-1} (inset figure: initial coulombic efficiency). d) Rate comparison performance. e) Cycling comparison performance at 100 mA g^{-1} . f) Charge/discharge curves of KFeHCF-E at 100 mA g^{-1} . g, h) Long-term cycle performance of KFeHCF-E at 500 mA g^{-1} , and 1000 mA g^{-1} , respectively.

shift slightly as the scan rate increases revealing the fast energy storage capability of KFeHCF-E. The capacitive contribution of KFeHCF-E gradually increases from 81% to 93% from 0.1 to 1.0 mV s^{-1} (Figure S13c, Supporting Information), showing that capacitance dominates the total capacity. While Figure S13d-f show the total capacity of KFeHCF dominated by diffusion controlled. This capacitance dominated energy storage process also reveals the fast K^+ storage process of KFeHCF-E. The galvanostatic intermittent titration technique (GITT) was used to investigate the ion insertion/extraction kinetics of the KFeHCF-E electrode at different current densities (Figures S14-S16, Supporting Information). The calculated K^+ diffusion coefficients for KFeHCF-E range from 10^{-13} to $10^{-9} \text{ cm}^2 \text{ s}^{-1}$ (Figure 5d) and are generally higher than that of KFeHCF. The observed larger voltage drop of KFeHCF-E than KFeHCF at low current densities is probably caused by ohmic resistance (Figure S14, Supporting Information), while lower voltage drop at high current densities probably derives from concentration and

electrochemical polarization (Figure S16, Supporting Information), which is strongly supported by smaller overpotential of KFeHCF-E at higher current densities (Figure S8).^[47] Therefore, the excellent rate performance of KFeHCF-E is mostly due to the high K^+ diffusion coefficient.

3. Conclusion

In conclusion, we report a simple aqueous coprecipitation method by introducing the chelator EDTA to slow down the crystallization process to prepare highly crystalline KFeHCF-E, which shows excellent electrochemical kinetics and high reversibility. The KFeHCF-E has a specific capacity (77 mAh g^{-1}), a high rate capability (60.9% capacity retention from 25 to 1000 mA g^{-1}), and an ultra-stable cyclability (61.3% capacity retention after 5000 cycles at 100 mA g^{-1}). In addition, a considerable capacity of 49.4 mAh g^{-1} and good cyclability can

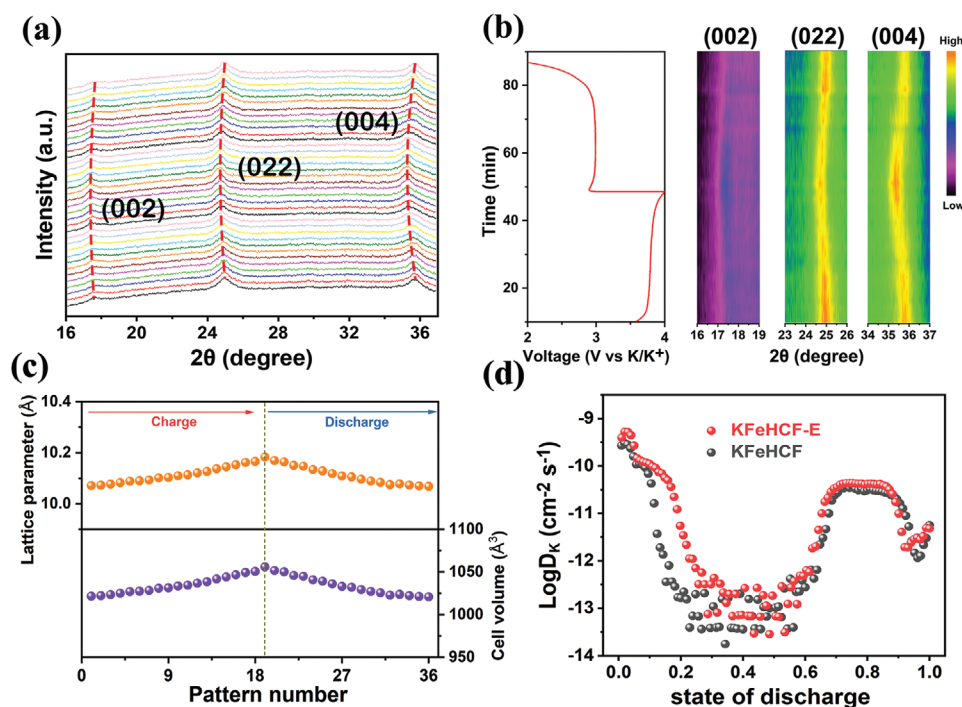


Figure 5. a) In situ XRD patterns of KFeHCF-E during the initial cycle. b) The corresponding charge/discharge curves and color-mapped curves for in situ XRD patterns for different angle ranges. c) The changes of KFeHCF-E lattice parameter and cell volume calculated by in situ XRD. d) GITT calculated the K-ion diffusion coefficient for both samples.

also be achieved at the high current density of 1000 mA g^{-1} . The excellent rate performance owes to fast K^+ insertion/extraction, which was determined by GITT and CV fitting. The slight lattice shrinkage/expansion upon K^+ insertion/extraction confirmed by in situ XRD is vital for the high structural stability of highly crystalline KFeHCF-E. In general, this work hopes to contribute to the investigation of highly crystalline PBAs for developments and applications of low-cost and long life-span KIBs.

4. Experimental Section

Materials Synthesis: The $\text{K}_2\text{Fe}[\text{Fe}(\text{CN})_6]$ samples were obtained by aqueous coprecipitation reactions at room temperature, all reagents used in this work were commercially available, and all deionized water was bubbled with nitrogen for 30 min. Typically, KFeHCF-E samples were synthesized at room temperature as follows: 100 mL containing 0.04 M ferrous sulfate ($\text{FeSO}_4 \cdot 7\text{H}_2\text{O}$, Aladdin) and 0.04 M ethylenediaminetetraacetic acid dipotassium salt dihydrate ($\text{EDTA} \cdot 2\text{K} \cdot 4\text{H}_2\text{O}$, Alfa) under continuous magnetic stirring and were added dropwise to 100 mL of 0.04 M potassium hexacyanoferric(II) trihydrate ($\text{K}_4\text{Fe}(\text{CN})_6 \cdot 3\text{H}_2\text{O}$, Aladdin) solution over 20 min under continuous magnetic stirring and N_2 bubbling. After aging for 4 h without stirring, the resulting precipitate was collected by centrifugation, washed several times with deionized water, and dried under vacuum at 80°C for 24 h. For comparison, control KFeHCF samples were obtained similarly but without the addition of $\text{EDTA} \cdot 2\text{K} \cdot 4\text{H}_2\text{O}$.

Materials Characterization: X-ray diffraction patterns (XRD) of these samples collected with D8 Advance powder X-ray diffraction with $\text{Cu K}\alpha$ ($\lambda = 1.5418 \text{ \AA}$). The corresponding voltage and current parameters were 20 kV and 10 A, respectively, and the test angle was $10\text{--}100^\circ$. The microscopic structures were characterized by scanning electron microscopy (SEM, JEOL JSM-7100F) equipped with energy dispersive

spectroscopy (EDS), high-resolution transmission electron microscopy (HRTEM, Titan G2-60-300 with image corrector) and High Angle Annular Dark Field (HAADF). X-ray photoelectron spectroscopy (XPS) analyses were investigated by using a VG Multilab 2000 system. Raman spectra were acquired with an excitation laser (532 nm) by using a Horiba LabRAM HR Evolution. Thermogravimetric measurements (Netzsch STA 449C) were performed under N_2 atmosphere from 30 to 400°C at a heating rate of 5°C min^{-1} to detect the content of water of crystallization. Raman spectra were recorded on a He-Ne laser instrument under 532 nm He-Ne laser excitation. The elemental contents were obtained by inductively coupled plasma (ICP, LEEMAN LABS Prodigy7) and elemental analyzer (Thermo Scientific Flash 2000). The crystal structure evolution and phase transition mechanisms during charge and discharge were analyzed using in situ X-ray diffraction (XRD). XRD signals were acquired every 120 s in still mode using a Bruker D8 Discover X-ray diffraction with the planar detector.

Electrochemical Characterizations: The electrochemical properties of the electrodes were measured in CR2016 coin cells. Typically, working electrodes are prepared by mixing 70 wt% PBA, 20 wt% super P, and 10 wt% polyvinylidene fluoride (PVDF) in 1-methyl-2-pyrrolidinone (NMP) to form a homogeneous slurry and then they were pasted on the aluminum foil. Subsequently, the coated aluminum foil is placed in a vacuum oven and dried at 120°C for 24 h. After that, the dried aluminum foil was further cut into small square sheets with a diameter of 10 mm and a thickness of 100 μm , where the average loading of PB was $\approx 1.0 \text{ mg cm}^{-2}$. The CR 2016-type coin cells were assembled in an argon-filled glove box (MIKROUNA, Super) with water and oxygen content below 0.01 ppm. Metal K and glass microfiber filter (Whatman, GF/D grade) were used as anode and separator, respectively. The electrolyte used was 2.5 M potassium bis(fluorosulfonyl)imide (KFSI) dissolved in triethyl phosphate (TEP). Constant current charge/discharge curves and cycling performance were carried out on the Neware battery test system (BTS 4000) at 25°C within the potential range of 2.0–4.0 V. Cyclic voltammetry (CV) at various scan rates and electrochemical impedance spectra (EIS) results between 0.01 Hz and 100 kHz were obtained on CORRTST electrochemical workstation (CS3105). The galvanostatic

intermittent titration technique (GITT) measurement proceeded via charge/discharge for 300 s followed by open-circuit relaxation for 1800 s on the Land battery test system (CT3002A).

Supporting Information

Supporting Information is available from the Wiley Online Library or from the author.

Acknowledgements

This work was supported by the Hainan Provincial Joint Project of Sanya Yazhou Bay Science and Technology City (520LH055, 2021CXLH0007), Hainan Innovative Postgraduate Research Project (Yhys2021-10), and the Sanya Science and Education Innovation Park of Wuhan University of Technology (2021KF0019, 2021KF0016).

Conflict of Interest

The authors declare no conflict of interest.

Data Availability Statement

The data that support the findings of this study are available from the corresponding author upon reasonable request.

Keywords

cathode materials, highly crystalline, Prussian blue, potassium ion battery, enhanced kinetics

Received: November 14, 2022
Revised: March 19, 2023
Published online:

- [1] S. Chu, Y. Cui, N. Liu, *Nat. Mater.* **2017**, *16*, 16.
- [2] B. Dunn, H. Kamath, J.-M. Tarascon, *Science* **2011**, *334*, 928.
- [3] P. E. Brockway, A. Owen, L. I. Brand-Correa, L. Hardt, *Nat. Energy* **2019**, *4*, 612.
- [4] L. Wang, J. Qiu, X. Wang, L. Chen, G. Cao, J. Wang, H. Zhang, X. He, *eScience* **2022**, *2*, 125.
- [5] C. Guo, Z. Liu, K. Han, L. Zhang, X. Ding, X. Wang, L. Mai, *Small* **2022**, *18*, 2107365.
- [6] Y. Wang, X. Yu, S. Xu, J. Bai, R. Xiao, Y.-S. Hu, H. Li, X.-Q. Yang, L. Chen, X. Huang, *Nat. Commun.* **2013**, *4*, 2365.
- [7] E. A. Olivetti, G. Ceder, G. G. Gaustad, X. Fu, *Joule* **2017**, *1*, 229.
- [8] S. Zhao, Z. Guo, K. Yan, X. Guo, S. Wan, F. He, B. Sun, G. Wang, *Small Struct.* **2021**, *2*, 2000054.
- [9] Y. Yang, J. Zhou, L. Wang, Z. Jiao, M. Xiao, Q. Huang, M. Liu, Q. Shao, X. Sun, J. Zhang, *Nano Energy* **2022**, *99*, 107424.
- [10] L. Deng, Z. Yang, L. Tan, L. Zeng, Y. Zhu, L. Guo, *Adv. Mater.* **2018**, *30*, 1802510.
- [11] Y. Guo, S. Wu, Y.-B. He, F. Kang, L. Chen, H. Li, Q.-H. Yang, *eScience* **2022**, *2*, 138.
- [12] S. Dhir, S. Wheeler, I. Capone, M. Pasta, *Chem* **2020**, *6*, 2442.
- [13] J. W. Choi, D. Aurbach, *Nat. Rev. Mater.* **2016**, *1*, 16013.
- [14] X. Min, J. Xiao, M. Fang, W. Wang, Y. Zhao, Y. Liu, A. M. Abdelkader, K. Xi, R. V. Kumar, Z. Huang, *Energy Environ. Sci.* **2021**, *14*, 2186.
- [15] D. Su, A. McDonagh, S.-Z. Qiao, G. Wang, *Adv. Mater.* **2017**, *29*, 1604007.
- [16] J. Ge, L. Fan, A. M. Rao, J. Zhou, B. Lu, *Nat. Sustainable* **2022**, *5*, 225.
- [17] S. Chong, Y. Wu, C. Liu, Y. Chen, S. Guo, Y. Liu, G. Cao, *Nano Energy* **2018**, *54*, 106.
- [18] J. Xie, X. Li, H. Lai, Z. Zhao, J. Li, W. Zhang, W. Xie, Y. Liu, W. Mai, *Angew. Chem., Int. Ed.* **2019**, *58*, 14740.
- [19] J. Xie, J. Li, X. Li, H. Lei, W. Zhuo, X. Li, G. Hong, K. N. Hui, L. Pan, W. Mai, *CCS Chem.* **2021**, *3*, 791.
- [20] L. Xu, W. Guo, L. Zeng, X. Xia, Y. Wang, P. Xiong, Q. Chen, J. Zhang, M. Wei, Q. Qian, *Chem. Eng. J.* **2021**, *419*, 129607.
- [21] T. Deng, X. Fan, C. Luo, J. Chen, L. Chen, S. Hou, N. Eidson, X. Zhou, C. Wang, *Nano Lett.* **2018**, *18*, 1522.
- [22] X. Wang, X. Xu, C. Niu, J. Meng, M. Huang, X. Liu, Z. Liu, L. Mai, *Nano Lett.* **2017**, *17*, 544.
- [23] J. Han, G.-N. Li, F. Liu, M. Wang, Y. Zhang, L. Hu, C. Dai, M. Xu, *Chem. Commun.* **2017**, *53*, 1805.
- [24] T. Hosaka, T. Shimamura, K. Kubota, S. Komaba, *Chem. Rec.* **2019**, *19*, 735.
- [25] X. Wu, Z. Jian, Z. Li, X. Ji, *Electrochem. Commun.* **2017**, *77*, 54.
- [26] J. Bie, K. Kubota, T. Hosaka, K. Chihara, S. Komaba, *J. Mater. Chem. A* **2017**, *5*, 4325.
- [27] H. Kim, H. Ji, J. Wang, G. Ceder, *Trends Chem.* **2019**, *1*, 682.
- [28] L. Xue, Y. Li, H. Gao, W. Zhou, X. Lü, W. Kaveevitchai, A. Manthiram, J. B. Goodenough, *J. Am. Chem. Soc.* **2017**, *139*, 2164.
- [29] H. Onuma, K. Kubota, S. Muratsubaki, T. Hosaka, R. Tatara, T. Yamamoto, K. Matsumoto, T. Nohira, R. Hagiwara, H. Oji, S. Yasuno, S. Komaba, *ACS Energy Lett.* **2020**, *5*, 2849.
- [30] C. Zhang, Y. Xu, M. Zhou, L. Liang, H. Dong, M. Wu, Y. Yang, Y. Lei, *Adv. Funct. Mater.* **2017**, *27*, 1604307.
- [31] J. Liao, Q. Hu, Y. Yu, H. Wang, Z. Tang, Z. Wen, C. Chen, *J. Mater. Chem. A* **2017**, *5*, 19017.
- [32] K. Hurlbutt, S. Wheeler, I. Capone, M. Pasta, *Joule* **2018**, *2*, 1950.
- [33] A. Zhou, W. Cheng, W. Wang, Q. Zhao, J. Xie, W. Zhang, H. Gao, L. Xue, J. Li, *Adv. Energy Mater.* **2021**, *11*, 2000943.
- [34] M. Qin, W. Ren, R. Jiang, Q. Li, X. Yao, S. Wang, Y. You, L. Mai, *ACS Appl. Mater. Interfaces* **2021**, *13*, 3999.
- [35] L. Deng, J. Qu, X. Niu, J. Liu, J. Zhang, Y. Hong, M. Feng, J. Wang, M. Hu, L. Zeng, Q. Zhang, L. Guo, Y. Zhu, *Nat. Commun.* **2021**, *12*, 2167.
- [36] L. Jiang, Y. Lu, C. Zhao, L. Liu, J. Zhang, Q. Zhang, X. Shen, J. Zhao, X. Yu, H. Li, X. Huang, L. Chen, Y.-S. Hu, *Nat. Energy* **2019**, *4*, 495.
- [37] S. Chong, Y. Wu, S. Guo, Y. Liu, G. Cao, *Energy Storage Mater.* **2019**, *22*, 120.
- [38] L. Li, Z. Hu, Y. Lu, C. Wang, Q. Zhang, S. Zhao, J. Peng, K. Zhang, S.-L. Chou, J. Chen, *Angew. Chem., Int. Ed.* **2021**, *60*, 13050.
- [39] Z. Wang, W. Zhuo, J. Li, L. Ma, S. Tan, G. Zhang, H. Yin, W. Qin, H. Wang, L. Pan, A. Qin, W. Mai, *Nano Energy* **2022**, *98*, 107243.
- [40] Y. Lin, J. Liu, L. Shi, N. Guo, Z. Sun, C. Geng, J. Jiang, Q. Zhuang, Y. Chen, Z. Ju, *J. Colloid Interface Sci.* **2022**, *623*, 1.
- [41] Y. You, X.-L. Wu, Y.-X. Yin, Y.-G. Guo, *Energy Environ. Sci.* **2014**, *7*, 1643.
- [42] M. Qin, W. Ren, J. Meng, X. Wang, X. Yao, Y. Ke, Q. Li, L. Mai, *ACS Sustainable Chem. Eng.* **2019**, *7*, 11564.
- [43] R. Chen, Y. Huang, M. Xie, Z. Wang, Y. Ye, L. Li, F. Wu, *ACS Appl. Mater. Interfaces* **2016**, *8*, 31669.
- [44] C. Gao, Y. Lei, Y. Wei, H. Wang, F. Yuan, F. Kang, D. Zhai, *Chem. Eng. J.* **2022**, *431*, 133926.
- [45] S. Chong, J. Yang, L. Sun, S. Guo, Y. Liu, H. K. Liu, *ACS Nano* **2020**, *14*, 9807.
- [46] J. Peng, W. Zhang, Z. Hu, L. Zhao, C. Wu, G. Peleckis, Q. Gu, J.-Z. Wang, H. K. Liu, S. X. Dou, S. Chou, *Nano Lett.* **2022**, *22*, 1302.
- [47] H. Peng, Y. Zhang, Y. Chen, J. Zhang, H. Jiang, X. Chen, Z. Zhang, Y. Zeng, B. Sa, Q. Wei, J. Lin, H. Guo, *Mater. Today Energy* **2020**, *18*, 100519.